Materials Today Communications 38 (2024) 107690

Contents lists available at ScienceDirect

Materials Today Communications

journal homepage: www.elsevier.com/locate/mtcomm

Remarkably enhanced corrosion performance of 316 L stainless steel via laser powder bed fusion thin-layer deposition

Jie Song [a,b], Kevin Sangoi [a], Mahdi Nadimi [a], Yao Fu [a,b,*]

[a] Department of Aerospace and Ocean Engineering, Virginia Polytechnic Institute and State University, USA
[b] Department of Materials Science and Engineering, Virginia Polytechnic Institute and State University, USA

ARTICLE INFO

Keywords:
Stainless steels
Laser-powder bed fusion
Pitting resistance
Pitting morphology

ABSTRACT

This study addresses the demand for on-demand repair and surface modification of conventional materials using advanced technology like laser powder bed fusion (L-PBF). The swift repair and enhancement of 316 L stainless steel surfaces are essential for various applications, especially in corrosive environments where component reliability and longevity are critical. This work aims to explore the improved corrosion properties of conventional 316 L using L-PBF by depositing a limited number of layers. It has been found that with a single- and double-layer deposition the corrosion resistance is improved significantly compared to that of the conventional 316 L. The pitting resistance of the 6-layer L-PBF deposit is comparable to the bulk counterpart.

1. Introduction

The austenistic 316 L stainless steel (SS) has been widely used in marine, nuclear and biomedical applications due to its relatively superior ductility and excellent corrosion resistant property over other materials. In addition, 316 L has desirable printability using laser-powder bed fusion (L-PBF) [1–8], due to its single-phase austenitic microstructures. It is well known that the L-PBF produces distinct microstructural features and defects from that of the conventional processes, which have been reported to contribute to the enhanced corrosion resistance of 316 L especially in sodium chloride solution [3,9–11]. The current work is motivated by the need of on-demand repair and surface modification of conventional 316 L via L-PBF. Thus, the conventional 316 L substrate is deposited with a limited number of printing layers: (a) single layer, (b) 2-layer with bidirectional scan of 0°, 90°, 67° rotation between subsequent layers, and (c) 6-layer with 67° rotation between subsequent layers, with the aim to understand the modified corrosion properties in comparison with their bulk conventional and L-PBF counterpart. The as-deposit features and corrosion characteristics are examined by advanced materials characterization and electrochemical analysis.

2. Materials and methods

AISI 316 L stainless steel powder (Fe-17Cr-12Ni-3Mo composition) from PRAXAIR was used to print the layers on an EOS M290 3D printer. The printer has a fixed laser diameter of 100 μm, and the Z-axis was designated as the build direction while the XY-plane served as the horizontal plane. Each layer had a uniform thickness of 20 μm, and a bidirectional scanning strategy was employed with rotations of 0°, 67°, and 90° between subsequent layers.

To prepare working electrodes for electrochemical tests, specimens were sealed with epoxy resin to expose a 0.32 cm^2 area and polished to a 0.05 μm colloidal silica surface. A three-electrode cell was used with a graphite counter electrode and an aqueous Ag/AgCl reference electrode. All potentials were referenced to the Ag/AgCl electrode. The solution employed was 3.5 wt% (0.61 M) NaCl at pH ≈ 5.8. Experiments were conducted at room temperature under natural aeration. Cyclic polarization curves followed the forward sweep rate of 0.1667 mV/s scan rate and reversed when reaching a current density of 0.5 mA/cm^2 at a reverse scan rate of 1.667 mV/s. Data was averaged from at least two measurements.

The microstructures of samples pre- and post-polarization were analyzed using scanning electron microscopy (SEM) and electron backscatter diffraction (EBSD). SEM/EBSD samples were electropolished with a 12.5 vol% sulfuric acid and 87.5 vol% methanol solution at 50 V and room temperature. Subsequently, the SEM sample was electrolytically etched in a 10 vol% saturated oxalic acid solution at 12 V for 90 s. To analyze the microstructure near the fusion boundaries, specimen across the fusion boundary was lifted out using the focused ion beam (FIB, FEI Helios 5). TEM observation was realized through JEOL

* Corresponding author at: Department of Aerospace and Ocean Engineering, Virginia Polytechnic Institute and State University, USA.
E-mail address: yaof@vt.edu (Y. Fu).

https://doi.org/10.1016/j.mtcomm.2023.107690
Received 16 November 2023; Accepted 23 November 2023
Available online 25 November 2023

JEM 2100 at 200 kV.

3. Results and discussions

The SEM image profile of the L-PBF deposit on the conventional 316 L SS substrate is depicted in Fig. 1. It reveals the presence of melt pool boundaries and cellular/columnar subgrains. It can be observed that the single-layer deposition layer has columnar subgrain growth of different orientations near the melt pool boundary (Fig. 1-a1 and a2). A mixture of cellular and columnar structure with different orientations are observed on this vertical plane in all conditions (Fig. 1a-e). The single-layer deposit measures approximately 80–100 μm in thickness. The two-layer, 0° rotation deposit experiences only a slight increase in layer thickness, whereas the 67° and 90° rotation deposits reach 120–130 μm. The six-layer deposit is estimated to be 150 μm, and it's evident that the earlier deposit layers underwent multiple remelting cycles due to deeper laser penetration than the individual layer thickness. Regardless of the number of deposit layers and rotation strategies, the deposits exhibit a consistent, very dense microstructure with a low level of porosity (<0.05).

A TEM sample was lifted out on the XY-plane identified in the 6-layer 67° rotation deposition sample, where the fusion boundary locates in the middle of the sample. The area scan across the boundary in Fig. 1-f2 indicates no segregation across the fusion boundary. Fig. 1-f3 shows the bright field image of the FIB specimen in the area indicated by the red box in Fig. 1-f1, where a grain boundary and high density of dislocation networks are identified. The fusion boundary location is not prominently featured in the bright field image. No inclusions or precipitates are identified around the fusion boundary.

The cyclic polarization curves conducted on the XY plane of the samples, along with the extracted corrosion properties such as pitting, repassivation, and corrosion potentials, are shown in Fig. 2. All L-PBF deposited surfaces demonstrate significantly improved pitting resistance, as evidenced by increased pitting potential. The degree of improvement depends on the number of deposit layers. For the conventional sample, the pitting potential measures approximately 310 mV. In contrast, the pitting potential for all samples with L-PBF deposit ranges from about 540 mV to 700 mV. Notably, the six-layer deposit at a 67° rotation exhibits the highest pitting potential.

When examining the repassivation and corrosion potentials, it becomes evident that there is no significant distinction between the potentials of the conventional sample and the L-PBF deposit sample (Fig. 2c). However, it is worth mentioning that the two-layer deposit at 90° and 0° rotations show lower values compared to all other samples. The repassivation potential for these two samples measures below 200 mV, while for all other samples, the repassivation potential is above 250 mV (Fig. 2c). Metastable pitting is most frequent with single-layer deposit but greatly reduced at the intermediate polarization potential at 2-layer deposit and minimal at the 6-layer deposit. This is in contrast to the repassivation and corrosion potential which do not exhibit clear dependency on the L-PBF condition.

The results of impedance measurements in 3.5% NaCl for L-PBF thin-layer deposits along with the conventional sample are depicted in Fig. 3. As shown in the bode plot (Fig. 3a), the impedance as a dependence of frequency exhibit similar trends for the different samples. The EIS result of the 6-layer 67° sample at E_{corr}, E_{corr}+ 100 mV, E_{corr}+ 200 mV, and E_{corr}+ 300 mV of anodic overpotential, shown in Fig. 3b, reveals that the capacitive loop increases in size when anodic polarization is applied (Nyquist plot). In general, in the Nyquist plot, a large semicircle implies difficulties in electron transfer between the substrate and solution, and the high capacitance of this loop implies a connection between two processes, the formation of the passive oxide layer and the charging of the electric double layer. This phenomenon resulted in a considerable rise in impedance at 0.001 frequency so that the sequence of impedance values is: $E_{corr} < E_{corr} + 100$ mv $< E_{corr} + 200$ mv $< E_{corr} + 300$ mv. The illustrated equivalent circuit (Fig. 3c) was used to model the electrochemical behavior. In this circuit, R_s represents the solution resistance, CPE is the double-layer capacitance and R_{ct} is the charge transfer resistance. Another aspect to consider is that at low frequencies of the Nyquist diagram, the mass transfer impedance appears as a line (Warburg impedance), which can contribute significantly to the overall internal resistance. Besides the 6-layer deposit, other L-PBF thin-layer deposit also showed the same pattern. As can be seen in Fig. 3d, with increasing potential over E_{corr}, the charge transfer resistance increased in all samples, indicating that the kinetics of the electrochemical process was slowed down (Fig. 3b and d). This increase is more significant for L-PBF thin-layer deposits, especially the sample with 67° rotation scan compared to the conventional sample. The value of R_{ct} at E_{corr} of all samples is almost the same (1–2 MΩ.cm^2). When the potential is 100, 200, and 300 mV above the E_{corr}, R_{ct} increases approximately by 2.5, 3, and 4.5 times, respectively, for L-PBF thin-layer deposit.

It is important to mention that the corrosion behavior of the L-PBF deposited samples all demonstrate that the formed passive layer is more resistant at 300 mV above the E_{corr}, indicating even greater resistance to anodic overpotential. This behavior could be attributed to the higher growth rate of passive film or higher passive layer thickness on the aforementioned samples. The single-layer deposit exhibits the highest R_{ct} at E_{corr} + 200 mV and E_{corr} + 300 mV. In contrast, the conventional sample contains merely passive film with the same resistance at best.

The surfaces exhibiting pitting, following polarization tests where backward scanning was halted at 0.5 mA/cm^2, were subjected to SEM and EBSD analysis, as shown in Fig. 4. A single major pit was found in all conditions. To enhance visibility, the fusion boundaries proximate to the pits were delineated by white lines. The pit morphology of the conventional sample displays an irregular shape, whereas that of the L-PBF deposit exhibits a more nearly round shape. All the pits feature broad openings and are relatively shallow. Notably, pitting in the L-PBF deposit does not exhibit a preference for growth along the fusion boundary; instead, it demonstrates an overall uniform growth in all directions. This inhomogeneity may stem from the dependence of corrosion properties on crystallographic orientation [12].

4. Discussion

The enhanced corrosion performance of L-PBF 316 L over its conventional counterpart has been well-reported before in NaCl solution [3,9–11,13,14]. However, there is still an active debate on the origin of improved properties of L-PBF sample. The main difficulty lies in the various types of different microstructural features (grain structure and phase constitution) and defects between the LBPF and conventional samples. These differences can be further altered when the processing parameters (e.g., laser powder, scan speed) are varied. The most popular mechanisms proposed for the improved corrosion performance in L-PBF condition include (1) The absence or very small-sized MnS inclusion [9] in L-PBF condition, and (2) the formation of a more compact and protective passive oxide film due to the high dislocation densities in the L-PBF 316 L [15,16], (3) the presence of porosity may cause metastable pitting event but not reduce the pitting resistance in dense L-PBF 316 L [17]. It is worth mentioning that, in the afore-mentioned studies, most if not all of the L-PBF conditions are considered in bulk form.

In this work, the conventional 316 L was L-PBF deposited by up to 6 layers, with an average thickness of a hundred microns. All L-PBF thin-layer deposit demonstrated remarkably increased pitting resistance. In contrast to previous reports [15,18,19], no chemical segregation has been found either around melt pool or within dislocation subgrain networks (Fig. 1f). The presence of such segregation has been reported to cause a microgalvanic coupling between the cellular interior and boundary [15,20,21].

The average equivalent grain size around the pit is larger in the 2-layer 0° rotation deposit compared to both that of single-layer deposit and the other 2-layer deposit (Fig. 4). The 6-layer 67° deposit exhibits the finest grain size (refer to Fig. 4). It is also noteworthy that the texture

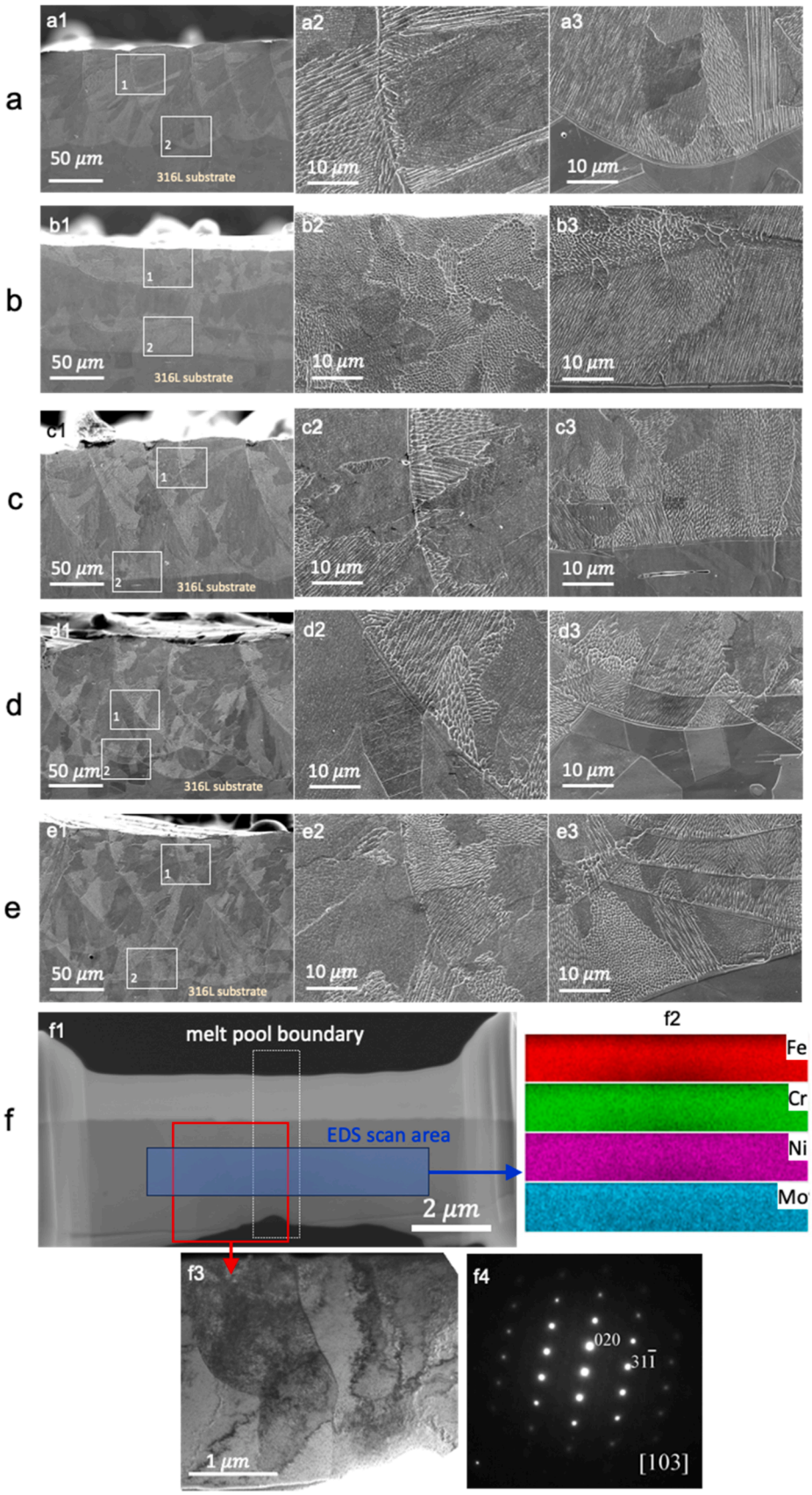

Fig. 1. SEM profile image of the (a) single layer deposition, (b) 2-layer 0° rotation deposition, (c) 2-layer 90° rotation deposition, (d) 2-layer 67° rotation deposition, (e) 6-layer 67° rotation deposition; subfigure 'X1′ and 'X2′ are the magnified area around melt pool boundary and deposit/substrate interface; (f) TEM analysis: (f1) FIB cross-section containing melt pool boundaries, (f2) EDS area scanning result of the blue line in f1. (f3) bright field images of the area in red rectangle in f1, (f4) SAD pattern of the 316L matrix.

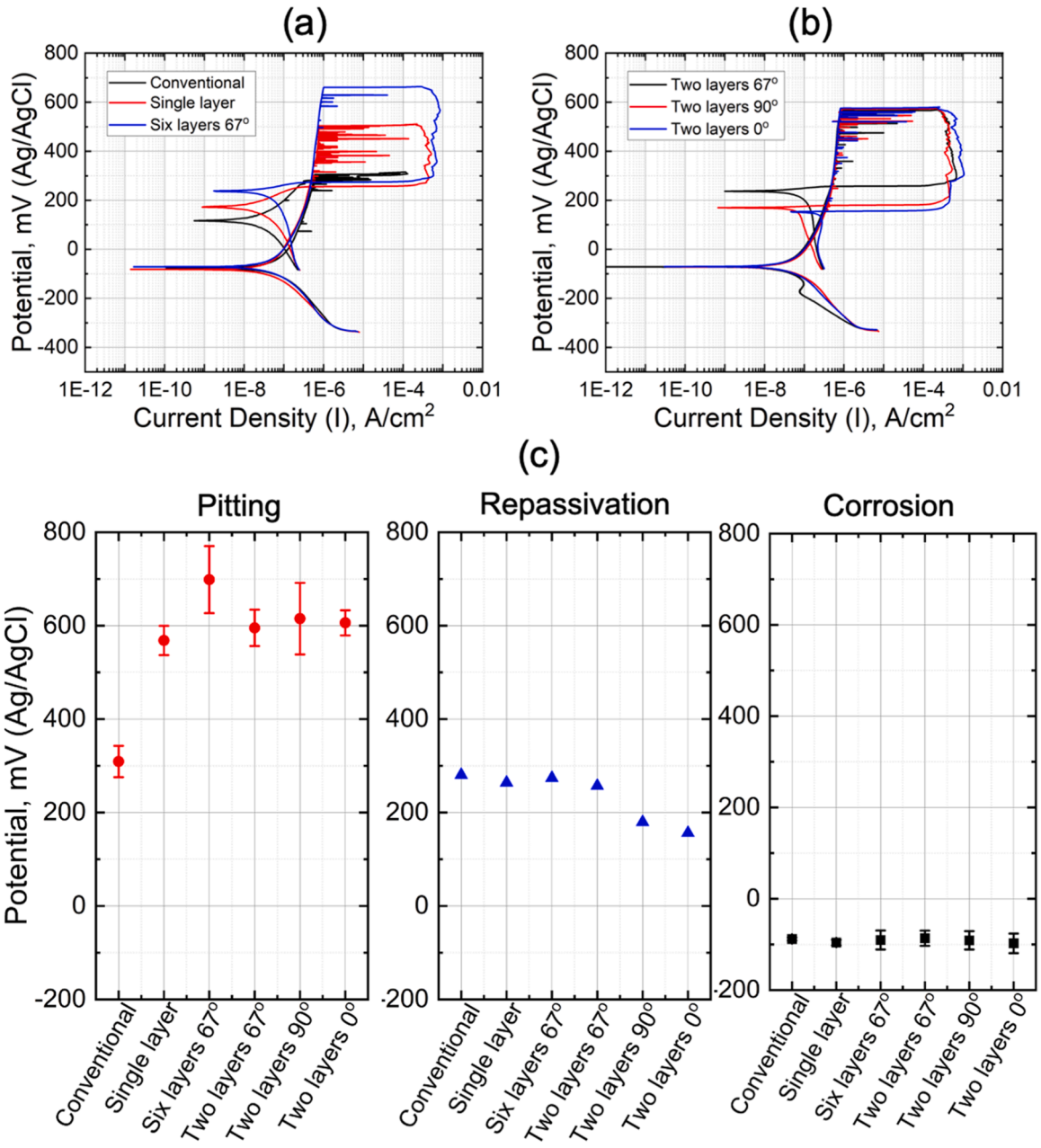

Fig. 2. Potentiodynamic curve of (a) the 316 L matrix, single- and 6- layer 67° rotation deposition, and (b) 2-layer 0°, 90°, and 67° rotation deposition, and (c) extracted pitting, repassivation, and corrosion potential.

has not yet developed in the sample with only 6 layers deposited. In contrast, the bulk sample with a 67° rotation scan displays a much coarser grain structure (grain diameter of 36.7 μm) and well-developed texture (see Fig. 5). Nevertheless, the pitting resistance of 6-layer deposit sample is comparable to that of the bulk L-PBF situation (700.5 mV vs. 748.3 mV), indicating a less significant role played by the grain size and texture.

The passive film resistance of the L-PBF layer deposit has been shown to increase more notably with polarization potential, in contrast to the conventional condition (Fig. 3d). Although it is challenging to directly relate the passive film resistance at E_{corr} + 300 mV to its breakdown at the pitting potential, as the passive film resistance declines at higher polarized potential [14], this difference between LBPF thin-layer deposit and the conventional counterpart supports the assumption that a higher density of cellular boundaries may increase reactivity by providing more sites for passive film nucleation. This, in turn, accelerates the formation of a protective layer on passivated alloys. This is also supported by the observation that the reduced metastable pitting event with an increasing number of deposit layers (Fig. 2a).

Limited studies have reported the pit morphology following polarization tests of L-PBF 316 L. Zhou et al. documented the melt pool boundary as the primary site of corrosion in the as-fabricated samples [22]. In contrast, Revilla found that the cellular boundary exhibits high resistance to attack compared to the cellular interior, thereby restricting the extent of penetration [23]. The pit morphology (Fig. 4 and Fig. 5) in this study demonstrate distinct features in that 1) the track boundary is not more susceptible to attack, 2) there is no apparent difference in the corrosion resistance between the cellular interior and boundary. The pit initiation occurs closely to the track boundary and grow more uniformly in all directions crossing the track/melt pool boundary. Crystallographic orientations can be visualized contributing to the local uneven growth. Finally, it is worth mentioning that the samples printed are highly dense

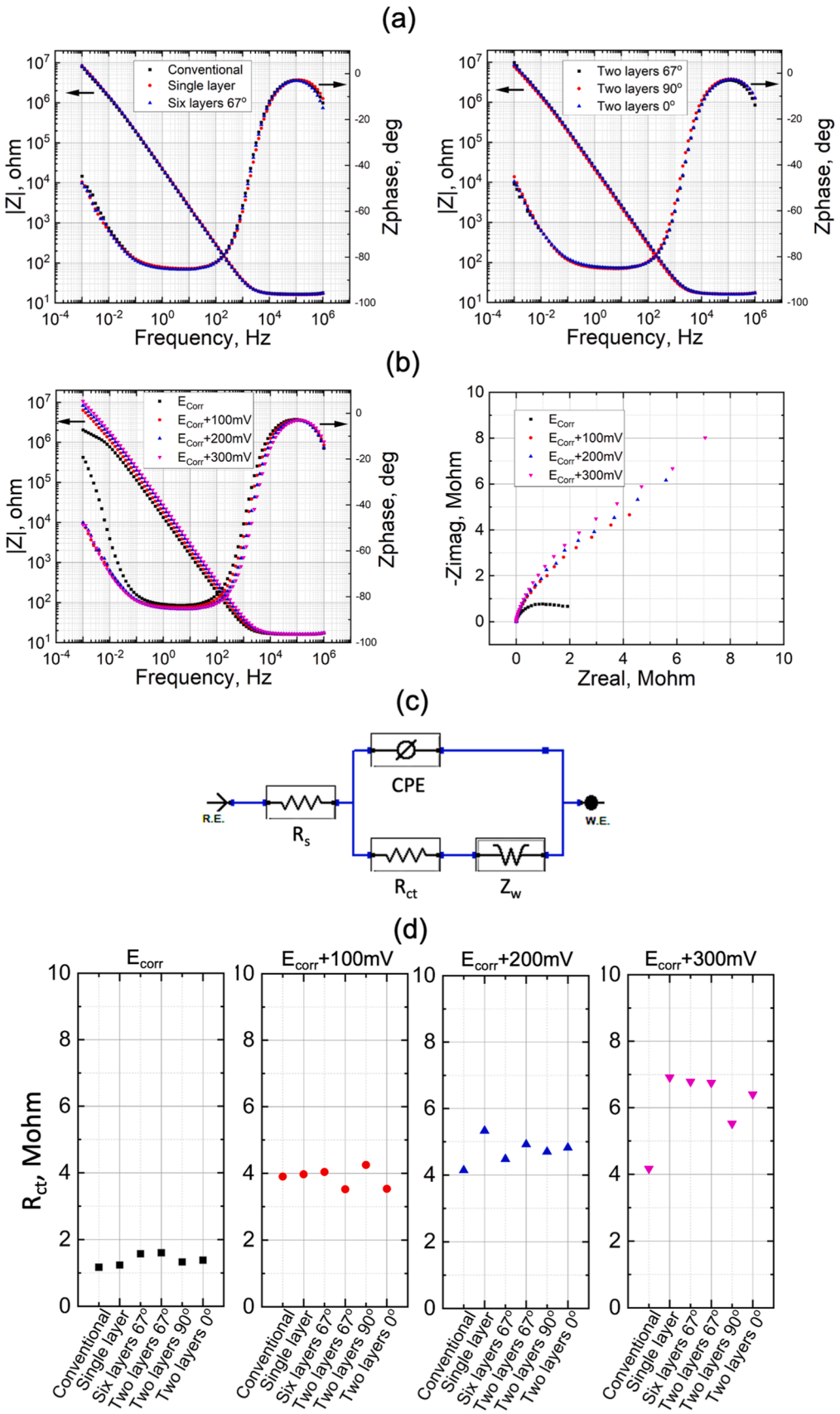

Fig. 3. EIS results of various 316 L samples, including conventional matrix, single layer, 6- layer 67° rotation, and 2-layer 0°, 90°, and 67° rotation deposition: (a) Bode plot at E_{corr}+ 300 mV, (b) Bode and Nyquist plot of the 6- layer 67° rotation 316 L at E_{corr}, E_{corr}+ 100 mV, + 200 mV and + 300 mV, respectively, (d) extracted charge transfer resistance (R_{ct}) using the equivalent circuit shown in (c).

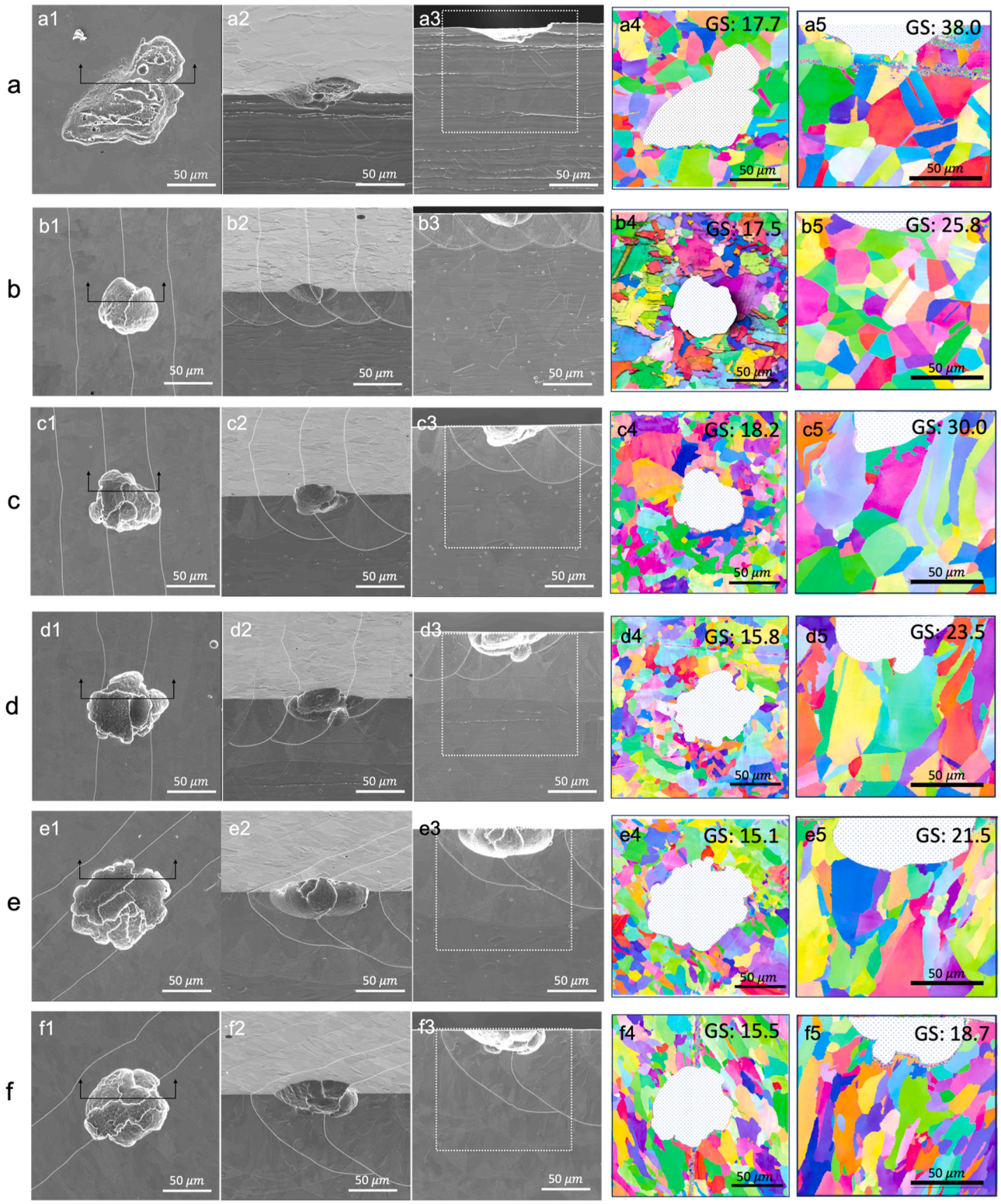

Fig. 4. SEM/EBSD image of the pit in the (a) conventional sample, (b) single layer deposition, (c) 2-layer 0° rotation deposition, (d) 2-layer 90° rotation deposition, (e) 2-layer 67° rotation deposition, (f) 6-layer 67° rotation deposition; X1-X3 are the SEM images viewed from the top (i.e., XY plane), 25° angle, and profile (i.e, YZ plane) of the selected cross section, respectively; X4 and X5 are the EBSD images of the selected domains in X1 and X3, respectively. The pits are shown in white in X4 and X5, as the signal selection fails within the pits, and GS represent the equivalent average grain diameter in μm.

and the examined surfaces are polished so that the porosity and surface roughness are not considered in this study.

5. Conclusions

Motivated by the need of on-demand repair and surface modification of conventional 316 L via L-PBF, we have investigated the conventional

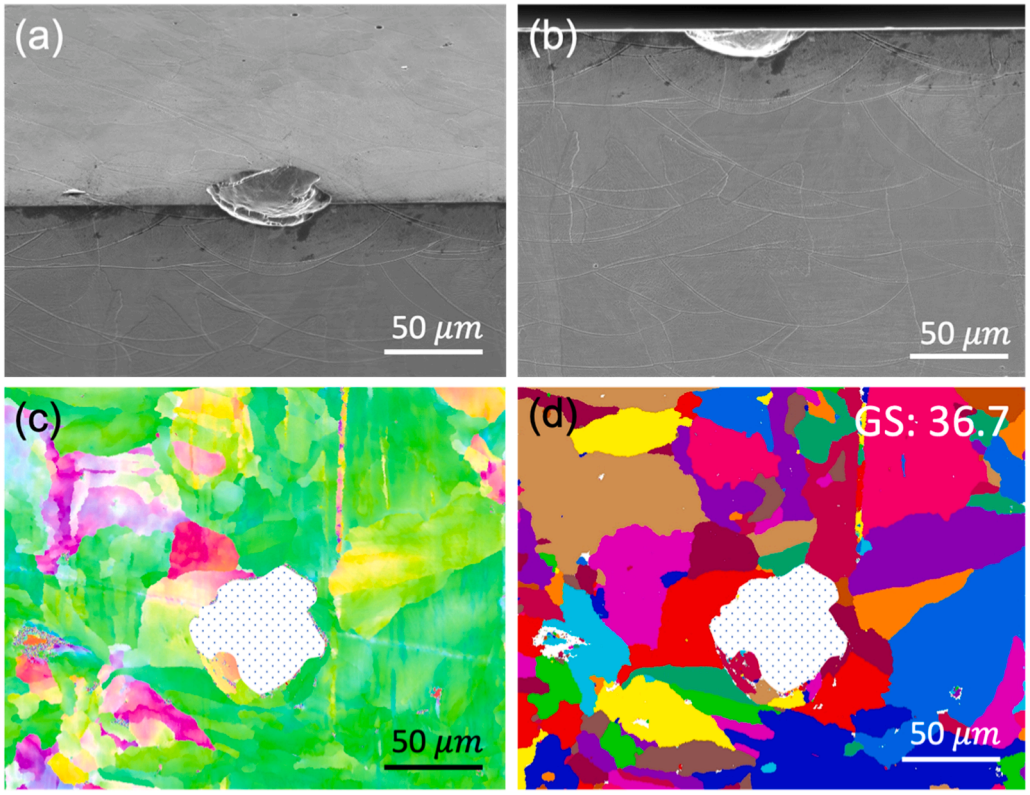

Fig. 5. SEM/EBSD image of the pit in the L-PBF 316 L bulk sample deposited with 67° rotation. The pits are shown in white in X4 and X5, as the signal selection fails within the pits, and GS represent the equivalent average grain diameter in μm.

316 L with single- to six- layer L-PBF deposit. The thickness of the deposit varies from 80 to 150 μm, depending on the number of deposit layer and scanning strategies. The conventional 316 L matrix is also investigated as comparison. We explore their microstructural features, passive film resistance, and corrosion properties and pitting morphology. This study addresses a gap in previous research, which predominantly focused on L-PBF 316 L in its bulk state. It paves the way for on-demand repair and surface modification of conventional 316 L components via L-PBF. The main conclusions are drawn as follows:

1. A single-layer L-PBF deposit can result in an approximately 300 mV increase in pitting resistance compared to conventional 316 L.
2. The pitting resistance of the 6-layer deposit is comparable to that of the bulk L-PBF counterpart, despite the more refined grain structure and yet-to-be-developed texture in the 6-layer deposit.
3. The passive film developed on the L-PBF thin-layer deposit is more resistant at the anodic potential compared to that of the conventional one.
4. The corroded surface after polarization test features one major pit that demonstrates a nearly round shape. No preferential growth along melt pool boundary and grain boundary are observed.
5. The enhanced pitting resistance is most likely attributed to the dense dislocation cellular/columnar subgrains developed during the L-PBF treatment.

CRediT authorship contribution statement

Jie Song: Conceptualization, Data curation, Formal analysis, Investigation, Methodology, Validation, Writing – original draft, Writing – review & editing. **Kevin Sangoi:** Formal analysis, Writing – original draft. **Mahdi Nadimi:** Formal analysis, Writing – original draft. **Yao Fu:** Conceptualization, Investigation, Resources, Supervision, Funding acquisition, Writing – review & editing.

Declaration of Competing Interest

The authors declare the following financial interests/personal relationships which may be considered as potential competing interests: Yao Fu reports financial support was provided by National Science Foundation and Office of Naval Research.

Data availability

Data will be made available on request.

Acknowledgment

The authors gratefully acknowledge the National Science Foundation (Award No. 2139383) and (Award No. 2245107), and Office of Naval Research (Award No. N00014–21-1–2800) for providing the financial support. This work utilized the Nanoscale Characterization and Fabrication Laboratory, a part of the National Nanotechnology Coordinated Infrastructure (NNCI), funded by NSF (ECCS 1542100 and ECCS 2025151).

References

[1] C. Qiu, M.A. Kindi, A.S. Aladawi, I.A. Hatmi, A comprehensive study on microstructure and tensile behaviour of a selectively laser melted stainless steel, Sci. Rep. 8 (2018) 7785.
[2] D. Gu, Y. Shen, Balling phenomena in direct laser sintering of stainless steel powder: metallurgical mechanisms and control methods, Mater. Des. 30 (2009) 2903–2910.
[3] S.-H. Sun, T. Ishimoto, K. Hagihara, Y. Tsutsumi, T. Hanawa, T. Nakano, Excellent mechanical and corrosion properties of austenitic stainless steel with a unique crystallographic lamellar microstructure via selective laser melting, Scr. Mater. 159 (2019) 89–93.
[4] J.A. Cherry, H.M. Davies, S. Mehmood, N.P. Lavery, S.G.R. Brown, J. Sienz, Investigation into the effect of process parameters on microstructural and physical properties of 316L stainless steel parts by selective laser melting, Int. J. Adv. Manuf. Technol. 76 (2015) 869–879.

[5] D. Wang, C. Song, Y. Yang, Y. Bai, Investigation of crystal growth mechanism during selective laser melting and mechanical property characterization of 316L stainless steel parts, Mater. Des. 100 (2016) 291–299.
[6] W.M. Tucho, V.H. Lysne, H. Austbø, A. Sjolyst-Kverneland, V. Hansen, Investigation of effects of process parameters on microstructure and hardness of SLM manufactured SS316L, J. Alloy. Compd. 740 (2018) 910–925.
[7] M. Yakout, M.A. Elbestawi, S.C. Veldhuis, On the characterization of stainless steel 316L parts produced by selective laser melting, Int. J. Adv. Manuf. Technol. 95 (2018) 1953–1974.
[8] Y.M. Wang, T. Voisin, J.T. McKeown, J. Ye, N.P. Calta, Z. Li, Z. Zeng, Y. Zhang, W. Chen, T.T. Roehling, R.T. Ott, M.K. Santala, Depond, J. Philip, M.J. Matthews, A.V. Hamza, T. Zhu, Additively manufactured hierarchical stainless steels with high strength and ductility, Nat. Mater. 17 (2017) 63.
[9] Q. Chao, V. Cruz, S. Thomas, N. Birbilis, P. Collins, A. Taylor, P.D. Hodgson, D. Fabijanic, On the enhanced corrosion resistance of a selective laser melted austenitic stainless steel, Scr. Mater. 141 (2017) 94–98.
[10] M.J.K. Lodhi, K.M. Deen, W. Haider, Corrosion behavior of additively manufactured 316L stainless steel in acidic media, Materialia 2 (2018) 111–121.
[11] F. Andreatta, A. Lanzutti, E. Vaglio, G. Totis, M. Sortino, L. Fedrizzi, Corrosion behaviour of 316L stainless steel manufactured by selective laser melting, Mater. Corros. 70 (2019) 1633–1645.
[12] P.T. Brewick, N. Kota, A.C. Lewis, V.G. DeGiorgi, A.B. Geltmacher, S.M. Qidwai, Microstructure-sensitive modeling of pitting corrosion: effect of the crystallographic orientation, Corros. Sci. 129 (2017) 54–69.
[13] J. Suryawanshi, T. Baskaran, O. Prakash, S.B. Arya, U. Ramamurty, On the corrosion resistance of some selective laser melted alloys, Materialia 3 (2018) 153–161.
[14] B. Gnanasekaran, J. Song, V. Vasudevan, Y. Fu, Corrosion fatigue characteristics of 316L stainless steel fabricated by laser powder bed fusion, Metals 11 (2021).
[15] D. Kong, C. Dong, X. Ni, L. Zhang, H. Luo, R. Li, L. Wang, C. Man, X. Li, The passivity of selective laser melted 316L stainless steel, Appl. Surf. Sci. 504 (2020), 144495.
[16] C. Man, C. Dong, T. Liu, D. Kong, D. Wang, X. Li, The enhancement of microstructure on the passive and pitting behaviors of selective laser melting 316L SS in simulated body fluid, Appl. Surf. Sci. 467–468 (2019) 193–205.
[17] G. Sander, S. Thomas, V. Cruz, M. Jurg, N. Birbilis, X. Gao, M. Brameld, C. R. Hutchinson, On the corrosion and metastable pitting characteristics of 316L stainless steel produced by selective laser melting, J. Electrochem. Soc. 164 (2017) C250–C257.
[18] D. Kong, C. Dong, S. Wei, X. Ni, L. Zhang, R. Li, L. Wang, C. Man, X. Li, About metastable cellular structure in additively manufactured austenitic stainless steels, Addit. Manuf. 38 (2021), 101804.
[19] P. Krakhmalev, G. Fredriksson, K. Svensson, I. Yadroitsev, I. Yadroitsava, M. Thuvander, R. Peng, Microstructure, solidification texture, and thermal stability of 316 L stainless steel manufactured by laser powder bed fusion, Metals 8 (2018).
[20] M. Cabrini, S. Lorenzi, T. Pastore, S. Pellegrini, M. Pavese, P. Fino, E.P. Ambrosio, F. Calignano, D. Manfredi, Corrosion resistance of direct metal laser sintering AlSiMg alloy, Surf. Interface Anal. 48 (2016) 818–826.
[21] M. Ziętala, T. Durejko, M. Polański, I. Kunce, T. Płociński, W. Zieliński, M. Łazińska, W. Stępniowski, T. Czujko, K.J. Kurzydłowski, Z. Bojar, The microstructure, mechanical properties and corrosion resistance of 316L stainless steel fabricated using laser engineered net shaping, Mater. Sci. Eng.: A 677 (2016) 1–10.
[22] C. Zhou, S. Hu, Q. Shi, H. Tao, Y. Song, J. Zheng, P. Xu, L. Zhang, Improvement of corrosion resistance of SS316L manufactured by selective laser melting through subcritical annealing, Corros. Sci. 164 (2020), 108353.
[23] R.I. Revilla, M. Van Calster, M. Raes, G. Arroud, F. Andreatta, L. Pyl, P. Guillaume, I. De Graeve, Microstructure and corrosion behavior of 316L stainless steel prepared using different additive manufacturing methods: a comparative study bringing insights into the impact of microstructure on their passivity, Corros. Sci. 176 (2020), 108914.